

Near-ideal Microwave Photon to Electron Conversion in a High Impedance Quantum Circuit

O. Stanisavljević,¹ J.-C. Philippe,¹ J. Gabelli,¹ M. Aprili,¹ J. Estève,¹ and J. Basset^{1,*}

¹*Université Paris-Saclay, CNRS, Laboratoire de Physique des Solides, 91405 Orsay, France*

(Dated: December 22, 2023)

Photoelectric detectors cover a wide frequency spectrum spanning from the far ultraviolet to the infrared light with high sensitivity, large quantum efficiency and low dark current. The equivalent photoelectric detection of microwave frequency photons has remained elusive due to inherent differences between microwave photon energy and the interband transition energies exploited in standard photoelectric detectors. Here we present the realization of a near-ideal microwave photon to electron converter at a frequency typical of circuit quantum electrodynamics. These unique properties are enabled by the use of a high kinetic inductance disordered superconductor, granular aluminium, to enhance the light-matter interaction. This experiment constitutes an important proof of concept regarding low energy microwave photon to electron conversion unveiling new possibilities such as the detection of single microwave photons using charge detection. It finds significance in quantum research opening doors to a wide array of applications, from quantum-enhanced sensing to exploring the fundamental properties of quantum states.

Introduction— Optical photon detectors are foundational tools in various quantum technologies and applications. The technology used by optical photon detection is based on semiconducting or superconducting materials whose energy gap appropriately matches the frequency domain of interest. Transferring this technology to microwave photons fails due to the natural mismatch between energy gap and microwave frequency photons which carry about 10^5 times less energy than an optical visible one. Alternative strategies using the circuit quantum electrodynamics toolbox have instead been used to detect single microwave photons [1–4]. Developing an efficient and fast photo-electron converter in the microwave domain remains a challenging task which holds immense promise in advancing microwave quantum optics [5] and sensing [6, 7], including axion detection [8, 9]. Several successful attempts have demonstrated the potential of using photoassisted tunneling in hybrid circuits combining semiconducting quantum dots with high finesse microwave cavities [10–13]. However, they demonstrated noticeable limitations in collecting efficiency, conversion efficiency and dark currents which constitute important challenges to overcome.

In this work we propose and implement a near-ideal microwave converter with large quantum efficiency (83%) and low dark count rate ($340 \times 10^3 \text{ s}^{-1}$). It is based on photon-assisted quantum tunnelling of quasiparticles in a voltage-biased superconducting tunnel junction [14–20] strongly coupled to a high impedance microwave resonator [1, 22]. The strong coupling regime is enabled by the use of granular aluminum (grAl), a high kinetic inductance disordered superconducting material with attractive material properties [23–28], to strengthen the light-matter coupling. In this approach the superconducting tunnel junction acts as a tuneable quantum absorber where the minimum number of absorbed photons per photoassisted tunneling (PAT) processes is set by the

voltage bias [20, 22]. Our work is complementary to previous works dealing with Cooper pairs tunneling in high impedance environments [29–34].

Principle of the experiment— The principle of the experiment is shown in figure 1. A dc biased superconducting tunnel junction is connected to a quarter wavelength resonator made of grAl with a high characteristic impedance. The microwave photons that we aim to convert into electrons are fed to the resonator by a microstrip 50Ω waveguide visible on the left of the figure 1(a). The photoassisted tunneling of one quasiparticle through the absorption of one photon from the resonator mode is energetically allowed if the bias voltage V verifies $eV > 2\Delta - \hbar\omega$, where Δ is the superconducting gap and ω the frequency of the resonator (see figure 1(b)). In the absence of photons, no dc current flows through the junction if $eV < 2\Delta$. The working voltage range of the detector is therefore $2\Delta - \hbar\omega < eV < 2\Delta$, where the dark current is low and the one photon photoassisted tunneling process allowed. The probability that an incoming photon is absorbed and converted into an electron defines the detector quantum efficiency, which reaches unity when the coupling rate κ_c from the resonator to the waveguide matches the absorption rate κ_J due to the photoassisted tunneling (PAT) process. This is equivalent to an impedance matching condition. Here, we have supposed for simplicity that other internal losses are negligible. The PAT rate coming from single photon absorption [1, 35–37] is given by

$$\kappa_J = \lambda^2 e^{-\lambda^2} I(V + \hbar\omega/e)/e \quad (1)$$

where the coupling constant $\lambda = \sqrt{\pi Z_C/R_K}$ is set by the ratio of the characteristic impedance of the mode Z_C to the quantum of resistance $R_K = h/e^2$ and $I(V)$ is the current voltage characteristic of the junction. In the experiment presented here, we designed our grAl resonator to reach $\lambda \sim 1$. The coefficient $\lambda^2 e^{-\lambda^2}$ corresponds to

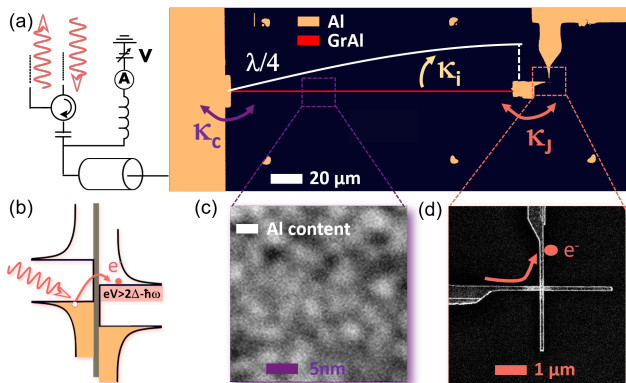


FIG. 1. **Principle of the experiment.** (a) Microscope image of the device and simplified schematic of the measurement setup. An incoming microwave photon is efficiently converted into an electron by coupling a waveguide to a high impedance resonator (red). Near ideal conversion is reached when the loss rate κ_J due to photoassisted tunneling through the junction matches the coupling rate κ_c to the input waveguide. The quarter wavelength resonator is made out of granular aluminum, the junction is aluminium based. (b) photoassisted tunneling of quasiparticles. The bias voltage sets a frequency band in which photons can be absorbed, while no elastic current flows through the junction. (c) Chemical content sensitive transmission electron microscope image of a granular aluminum thin film. Brighter colors means larger aluminium content. Darker areas have a stronger oxygen content. (d) Scanning electron microscope image of the superconducting tunnel junction.

the Franck-Condon matrix element $|\langle 0|D_\lambda|1\rangle|^2$, where D_λ is the displacement operator $\exp(i\lambda(a+a^\dagger))$, which translates the charge degree of freedom of the resonator mode a by one electron [35]. Connecting the resonator to a $50\ \Omega$ waveguide typically leads to a coupling rate $\kappa_c \sim 2\pi \times 50\ \text{MHz}$ (see supplementary informations (S.I.)). A straightforward estimate based on equation (1) indicates that a junction with a resistance of about $1\ \text{M}\Omega$ fulfills the impedance matching condition in the detector bias window (see S.I.). This large value of the tunnel junction resistance is highly beneficial to reduce the probability of elastic tunneling and therefore the dark current, which is a key figure of merit. In a conventional low impedance resonator, the Franck-Condon factor $\lambda^2 e^{-\lambda^2}$ would reduce the photoassisted tunneling rate by approximately two orders of magnitude. The matching condition could still be reached, but with a much more transparent junction, which is detrimental in terms of dark current.

The sample shown in figure 1 is fabricated via a three steps process using standard e-beam and optical lithography techniques. It is then mounted in a dilution fridge with a base temperature of 20 mK with a measurement circuit which allow for both dc-biasing the tunnel junction, feeding microwaves and measure the sample microwave reflection S_{11} . The measured sample has a characteristic impedance of $5.1\ \text{k}\Omega$, $\lambda = 0.79$, and a large normal state resistance junction $1.53\ \text{M}\Omega$ obtained by triple oxidation (see S.I.).

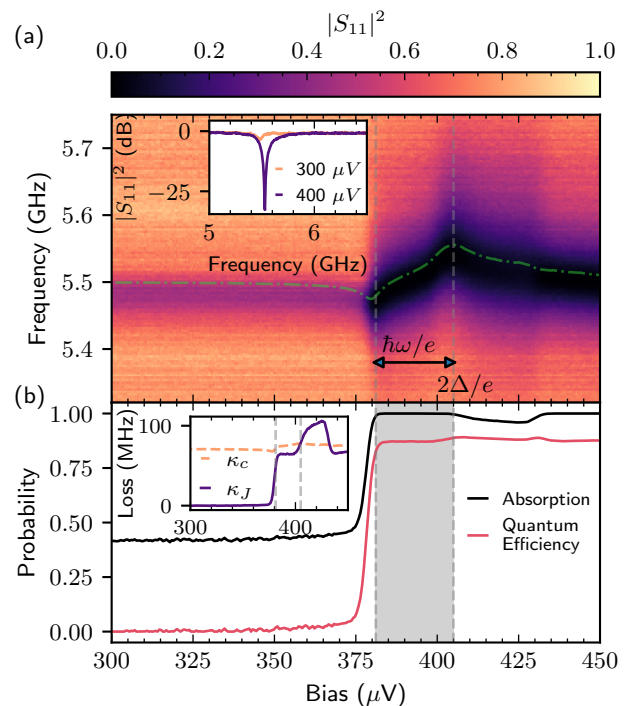


FIG. 2. **Microwave spectroscopy.** (a) Squared modulus $|S_{11}|^2$ of the microwave reflection coefficient near resonance vs frequency and bias voltage. The resonance frequency is shown as a green dash-dotted line and undergoes Lamb shift. Inset: Frequency linecuts for two significant voltages (reference and critical coupling spectra). (b) Probability of microwave absorption and quantum efficiency expected from spectroscopic measurements. The efficiency is steadily beyond 80% over a broad bias window especially when $2\Delta - \hbar\omega < eV < 2\Delta$ where a small dark current is expected. Inset: Voltage bias dependence of the loss rates κ_c and κ_J .

Microwave spectroscopy— We show in figure 2(a) a colormap of the reflection coefficient $|S_{11}|^2$ of the resonator as a function of frequency and bias voltage in the vicinity of the superconducting gap $2\Delta/e$. The power of the probe tone is sufficiently low to be in the linear regime, where the measured spectrum is power independent. Below $340\ \mu\text{V}$, where no current is expected to flow through the junction, even in the presence of microwave, the reflection coefficient S_{11} exhibits a resonance around $\omega/2\pi = 5.525\ \text{GHz}$ with a small dissipative response (-2dB dip, see inset), indicating that the internal losses of the resonator are much smaller than κ_c as desired. When the voltage increases toward the gap and eV reaches $2\Delta/e - \hbar\omega$ (gray shaded area), photons are absorbed by the junction through photoassisted electron tunneling. The reflection dip correspondingly becomes more pronounced (inset figure 2(a)). Additionally, the resonance frequency shifts (dotted-dashed green line in figure 2(a)) due to the coupling to the junction as a consequence of Kramers-Krönig relations [17, 18, 22]. At a

given voltage, we fit the reflection S_{11} using

$$S_{11} = 1 - \frac{\kappa_c}{\kappa/2 + \kappa_c/2 + i(\omega_p - \omega)}. \quad (2)$$

where ω_p is the pump frequency and ω , κ_c and κ three fitting parameters. The loss rate κ is the sum of the PAT loss rate κ_J and other intrinsic losses with a rate κ_i . We determine $\kappa_i = 2\pi \times 9.5$ MHz by taking the averaged value of κ for $V < 380$ μ V where $\kappa_J \approx 0$. We then assume that κ_i is voltage independent and obtain $\kappa_J = \kappa - \kappa_i$. The evolution of κ_c and κ_J as a function of voltage is shown in the inset of figure 2(b). From these values, we compute the probability that an incoming photon at resonance is absorbed $1 - |S_{11}(\omega_p = \omega)|^2 = 1 - (\kappa - \kappa_c)^2/(\kappa + \kappa_c)^2$ (see figure 2(b)). Critical coupling, which corresponds to perfect absorption ($|S_{11}|^2 = 0$), is reached when $\kappa_J = \kappa_c - \kappa_i$. We observe a minimal reflection below -30 dB at the corresponding voltage (inset figure 2(a)). We can estimate the quantum efficiency by noting that the resonator population at resonance is $n_{\text{ph}} = 4\phi\kappa_c/(\kappa_J + \kappa)^2$ where ϕ is the incoming photon flux. The quantum efficiency is then $\kappa_J n_{\text{ph}}/\phi = 4\kappa_J\kappa_c/(\kappa_J + \kappa)^2$, which we also plot in figure 2(b). It is maximal when $\kappa_J = \kappa_c + \kappa_i$, which happens at a voltage slightly above critical coupling. The expected efficiency is steadily beyond 80% over the full working window $2\Delta - \hbar\omega < eV < 2\Delta$ of the detector (gray area).

Photoassisted tunneling current from coherent pumping— In order to verify that the losses induced by the junction indeed correspond to the conversion of photons into electrons, we measure the PAT current I_{PAT} as a function of the incident microwave power. Figure 3(a) shows the power dependence of the current-voltage characteristics $I(V)$ when shining a microwave tone at the resonance frequency ω . As the power increases, a first subgap current step emerges that grows linearly with pump strength. Additional steps appear at higher power that correspond to multiphoton absorption processes. Because of energy conservation, processes where N photons are absorbed to photoassist the tunneling of one electron are allowed when $eV > 2\Delta - N\hbar\omega$. The coloured bands indicate the process with minimal N allowed at each step. We measure the photocurrent at the center of the first four steps and plot their evolution with power in figure 3(b). The plotted I_{PAT} corresponds to the difference between the current with and without microwaves, not taking into account the dark current, which will be addressed later. At the $N = 1$ step, the ratio between I_{PAT}/e and the photon flux $\phi = P/\hbar\omega$, where P is the incident power on the detector, is the quantum efficiency χ , which should match the value of 83% estimated above.

A precise direct measurement of χ is known to be difficult because of the unavoidable uncertainty on the value of the attenuation of the microwave source and the detector in the cryostat. In the limit $n_{\text{ph}} \ll 1$, the PAT

current at step N is given by the population in the N Fock state multiplied by the rate $|\langle 0|D_\lambda|n\rangle|^2 \times I(2\Delta + \hbar\omega/2)/e$. The population is given by $(\phi/\kappa_N)^N$ where κ_N is an effective loss rate, which depends on κ_c , κ , λ and $I(V)$ and can be calculated analytically (see S.I.).

Fixing κ_c to the previously measured value, $\lambda = 0.79$, and using the independently measured resistance of the junction to estimate $I(2\Delta + \hbar\omega/2)/e$, the four I_{PAT} curves can be fitted with the attenuation as a single free parameter, which is very constrained because each curve is proportional to the N -th power of the attenuation. Because we are not deeply enough in the $n_{\text{ph}} \ll 1$ regime, the fitting procedure is a bit more elaborate and relies on the numerical simulation of the Lindblad master equation describing the dynamics of the resonator mode instead of the analytical expressions (see S.I.). We obtain an attenuation of $-107.0 \text{ dB} \pm 0.3 \text{ dB}$, corresponding to $\chi = 0.83$. The resulting simulated I_{PAT} curves are shown as solid lines in figure 3(b). The good quality of the fit for all the steps at once with a single adjustable parameter confirms our good understanding of the PAT processes. We estimate the systematic uncertainty on the quantum efficiency to be on the order of 0.05.

The deduced attenuation factor is only 1.0 dB above the estimated value that we obtain from an independent measurement of the overall transmission of the microwave lines of the cryostat and 0.2 dB above the one obtained by shot-noise calibration (see S.I.). At large power, the detector saturates when n_{ph} becomes on the order of unity and multiphoton processes cannot be neglected. More specifically the 1 dB (3 dB) compression points occur respectively for $P = -119.0$ (-114.2) dBm or $\phi = 340$ (1036) Mph/s, at which we estimate $n_{\text{ph}} = 0.57$ (5.37).

Photoassisted current from thermal population— As an independent test of our estimate of the quantum efficiency, we measure the blackbody radiation coming from the matched 50Ω load that is connected to the circulator port in direct view of the detector (see detailed circuit in S.I.). We suppose that the load is thermalized to the fridge temperature. In the limit $n_{\text{ph}} \ll 1$, the temperature dependent resonator population reads $n_{\text{ph}}(T) = (\kappa_c + \kappa_i)/(\kappa_c + \kappa_i + \kappa_J)n_{\text{BE}}(T)$ with the Bose-Einstein distribution $n_{\text{BE}}(T) = 1/(\exp(\hbar\omega/k_B T) - 1)$. This assumes that the coupling and intrinsic loss channels both connect the resonator to a bath at temperature T and that the junction behaves as a zero temperature bath. The corresponding thermally photoassisted current is $e\kappa_J n_{\text{ph}}$. Here, we do measure the total current, which is given by $I_{\text{D}} + e\kappa_J n_{\text{ph}}$, where I_{D} is the dark current of our detector. Figure 4 shows the measured current-voltage traces (inset) and photoassisted current while the bias voltage is set in the middle of the $N = 1$ step as a function of temperature from 20 to 150 mK. The full line corresponds to the

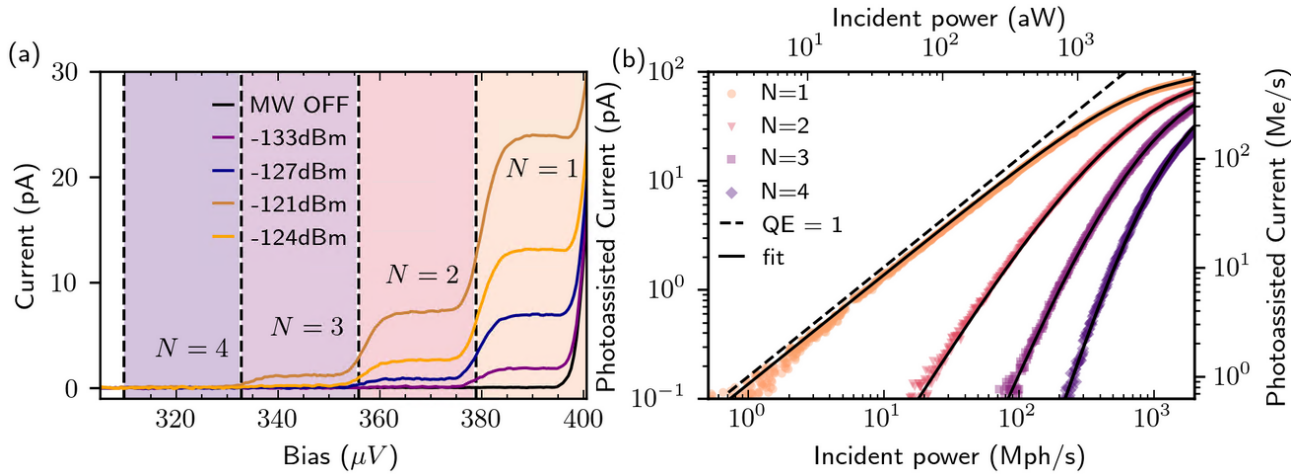


FIG. 3. **Photoassisted current and quantum efficiency.** (a) Voltage dependence of the subgap current for different microwave powers at frequency $\omega/2\pi = 5.525$ GHz. At low power, a single step is observed when $2\Delta - \hbar\omega < eV < 2\Delta$ corresponding to a PAT current where one photon gives one electron. At higher powers, multi-photon processes involving the tunneling of a single electron with N absorbed photons occur when $eV > 2\Delta - N\hbar\omega$. (b) Power dependence of the $N = 1, 2, 3, 4$ PAT current steps at resonance frequency $\omega/2\pi = 5.525$ GHz and the corresponding theoretical prediction (see S.I.).

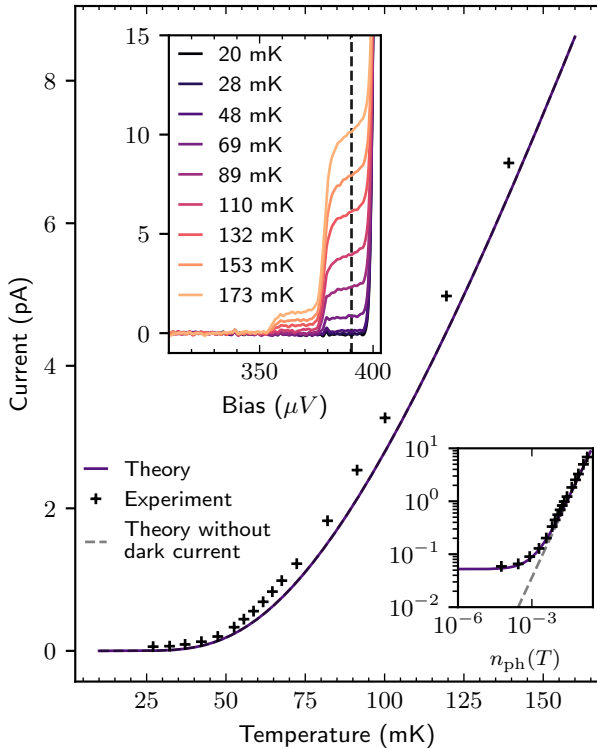


FIG. 4. **Thermal photoassisted current and dark current.** Temperature dependence of the current measured at the center of the $N = 1$ photo-current step (dashed line in top inset). The full line is the expected current using the values of the loss rates fitted in figure 1 to which is added the measured dark current. Top inset: Voltage dependence of the subgap current for different temperatures. Lower inset: same data as main in a logarithmic scale vs the thermal occupation $n_{\text{th}}(T)$. The saturation at low temperature is due to the dark current of our detector.

expected thermal photocurrent only ($e\kappa_J n_{\text{ph}}$) with a non zero dark current $I_D = 55$ fA while the dashed line emphasizes the expected photocurrent alone. Again, the agreement between the simple prediction using the loss rates obtained from the resonator spectroscopy and the measured current is good without any adjustable parameters. The small discrepancy can be reduced if we consider the sample temperature is $\approx 5\%$ above the one measured by the thermometer. The origin of the dark current is unclear. We show in S.I. its voltage dependence which indicates that dark current is not due to a rounding of the $I(V)$ of the junction near the gap, but rather to a non equilibrium population of the resonator modes at ω and 3ω which we estimate to $n_{\text{ph}} = 1.10^{-3}$ (2.10^{-4}) at ω (3ω).

Noise Equivalent Power— In the data presented here, the current is measured using a differential voltage amplifier on a 51.6 k Ω resistor in series with the junction. The equivalent current noise of this setup is 120 fA/ $\sqrt{\text{Hz}}$, which results in a Noise Equivalent Power (NEP) of 2.7×10^{-18} W/ $\sqrt{\text{Hz}}$. The setup could be modified in order to reduce the current noise measurement to 0.1 fA/ $\sqrt{\text{Hz}}$ by using a HEMT voltage amplifier [38], reducing the NEP to 2.3×10^{-21} W/ $\sqrt{\text{Hz}}$.

Conclusion— We have realized an important proof of concept regarding low energy microwave photon to electron conversion using high impedance quantum circuits unveiling new possibilities. The quantum efficiency of the process is unprecedentedly high (83%) compared to the state of the art [11] and is limited by the internal quality of the grAl resonator, which has been shown by others to be high [25]. The relatively large intrinsic losses of the sample is of unknown origin. Other resonators fabricated with the same technique have shown significantly larger intrinsic quality factor (about two times). Quan-

tum efficiency as large as 99% should be within reach of this technique by increasing the intrinsic quality factor above 10^4 . The detected frequency, here around 6 GHz, could be increased until twice the superconducting gap, where other types of superconducting detectors, for example kinetic inductance detectors, become efficient. On the lower side, the frequency could also be lowered, which will most likely result in a larger dark current. The quantum efficiency will remain high as long as the different steps in the photocurrent are well resolved. The high quantum efficiency and the low dark current are promising regarding single photon detection by combining our detector with a radiofrequency single electron transistor [39]. We estimate that given the charge sensitivity of state-of-the-art single electron transistor, single photons could be measured at a maximal rate of 100 kHz. This will require to lower the detection bandwidth (κ_c) and increase the junction resistance in order to reduce the dark counts. The recent work in [6] shows that dark count rates as low as 100 Hz can be reached in a narrow band detector. We believe our microwave photon-to-electron converter will play a pivotal role in advancing quantum technology and anticipate applications ranging from spin sensing to dark matter search.

Acknowledgements— We thank R. Deblock, C. Quay Huei Li, A. Palacio-Morales, for stimulating discussions, C. Di Giorgio for her help in cabling the dilution fridge, L. Galvao-Tizei for TEM images. We acknowledge financial support from the ANR (ANR-21-CE47-0010 KIMIDET project and ANR-18-CE47-0003 BOCA project), from the France 2030 plan under the ANR-22-PETQ-0003 RobustSuperQ grant, from the Région Île-de-France in the framework of DIM SIRTEQ (Science et Ingénierie en Région Île-de-France pour les Technologies Quantiques) and the Laboratoire d'excellence Physique Atomes Lumière Matière (ANR-10-LABX-0039-PALM).

* julien.basset@universite-paris-saclay.fr

- [1] Sathyamoorthy, S.R., Stace, T.M., Johansson G., Detecting itinerant single microwave photons. *Comptes Rendus. Physique*, Tome 17 (2016) no. 7, pp. 756-765. doi : 10.1016/j.crhy.2016.07.010. <https://comptes-rendus.academie-sciences.fr/physique/articles/10.1016/j.crhy.2016.07.010/>
- [2] Inomata, K., Lin, Z., Koshino, K. et al. Single microwave-photon detector using an artificial Λ -type three-level system. *Nat Commun* 7, 12303 (2016).
- [3] Besse, J.-C. et al. Single-shot quantum nondemolition detection of individual itinerant microwave photons. *Phys. Rev. X* 8, 021003 (2018).
- [4] Lescanne, R., et al. Irreversible Qubit-Photon Coupling for the Detection of Itinerant Microwave Photons, *Phys. Rev. X* 10, 021038 (2020)
- [5] Blais, A., Grimsmo, A.L., Girvin, S.M., Wallraff, A. Circuit quantum electrodynamics. *Reviews of Modern Physics* 93 (2), 025005 (2021)
- [6] Albertinale, E., Balembois, L., Billaud, E. et al. Detecting spins by their fluorescence with a microwave photon counter. *Nature* 600, 434–438 (2021). <https://doi.org/10.1038/s41586-021-04076-z>
- [7] Wang, Z., Balembois, L., Rančić, M. et al. Single-electron spin resonance detection by microwave photon counting. *Nature* 619, 276–281 (2023). <https://doi.org/10.1038/s41586-023-06097-2>
- [8] Sikivie, P. Invisible axion search methods. *Rev. Mod. Phys.* 90, 015004 (2021).
- [9] Pankratov, A.L., Revin, L.S., Gordeeva, A.V. et al. Towards a microwave single-photon counter for searching axions. *npj Quantum Inf* 8, 61 (2022). <https://doi.org/10.1038/s41534-022-00569-5>
- [10] Wong, C.H. and Vavilov, M. G. Quantum efficiency of a single microwave photon detector based on a semiconductor double quantum dot, *Phys. Rev. A* 95, 012325 (2017).
- [11] Khan, W. et al. *Efficient and continuous microwave photoconversion in hybrid cavity-semiconductor nanowire double quantum dot diodes*, *Nature Communications* 12, 5130 (2021).
- [12] Cornia, S. et al. , Calibration-free and high-sensitivity microwave detectors based on inas/inp nanowire double quantum dots, *Adv. Funct. Mater.* , 2212517 (2023).
- [13] Haldar, S. et al. Microwave power harvesting using resonator-coupled double quantum dot photodiode. *arXiv:2306.15797* (2023)
- [14] Dayem, A. H., and Martin, R. J., Quantum Interaction of Microwave Radiation with Tunneling Between Superconductors, *Phys. Rev. Lett.* 8, 246 –(1962)
- [15] Tien, P. K. and Gordon, J. P. Multiphoton process observed in the interaction of microwave fields with the tunneling between superconductor films. *Phys. Rev.* 129, 647–651 (1963).
- [16] Tucker, J. R. and Feldman, M. J. Quantum detection at millimeter wavelengths. *Rev. Mod. Phys.* 57, 1055–1113 (1985)
- [17] Worsham, A.H. et al. Quantum tunneling currents in a superconducting junction. *Phys. Rev. Lett.* 67, 3034–3037 (1991).
- [18] Basset, J., Bouchiat, H. and Deblock, R., High-frequency quantum admittance and noise measurement with an on-chip resonant circuit. *Phys. Rev. B* 85, 085435 (2012).
- [19] Tan, K. et al. Quantum-circuit refrigerator. *Nature Communications* 8, 15189 (2017).
- [20] Viitanen, A. et al. Quantum-circuit refrigeration of a superconducting microwave resonator well below a single quantum, *arXiv:2308.00397* (2023).
- [21] Estève, J., Aprili, M., and Gabelli, J., Quantum dynamics of a microwave resonator strongly coupled to a tunnel junction. *arXiv:1807.02364* (2018)
- [22] Aiello, G., et al. Quantum bath engineering of a high impedance microwave mode through quasiparticle tunneling, *Nature Communications* 13, 7146 (2023).
- [23] Annunziata, A. J. et al. Tunable superconducting nanoinductors. *Nanotechnology* 21, 445202 (2010)
- [24] Samkharadze, N. et al. High-kinetic-inductance superconducting nanowire resonators for circuit QED in a magnetic field. *Phys. Rev. Appl.* 5, 044004 (2016)
- [25] Grünhaupt, L. et al. Loss mechanisms and quasiparticle dynamics in superconducting microwave resonators made of thin-film granular aluminum. *Phys. Rev. Lett.* 121, 117001 (2018).

- [26] Maleeva, N. et al. Circuit quantum electrodynamics of granular aluminum resonators. *Nat. Commun.* 9, 1–7 (2018).
- [27] Kamenov, P. et al. Granular aluminum meandered superinductors for quantum circuits. *Phys. Rev. Appl.* 13, 054051 (2020).
- [28] Glezer Moshe, A., Farber, E. and Deutscher, G. Granular superconductors for high kinetic inductance and low loss quantum devices. *Appl. Phys. Lett.* 117, 062601 (2020)
- [29] Chen, Y.-F. et al. Microwave Photon Counter Based on Josephson Junctions. *Phys. Rev. Lett.* 107, 217401 – Published 14 November 2011
- [30] Leppäkangas, J. et al. Multiplying and detecting propagating microwave photons using inelastic Cooper-pair tunneling. *Phys. Rev. A* 97, 013855 – Published 31 January 2018
- [31] Jebari, S., Blanchet, F., Grimm, A. et al. Near-quantum-limited amplification from inelastic Cooper-pair tunnelling. *Nat Electron* 1, 223–227 (2018). <https://doi.org/10.1038/s41928-018-0055-7>
- [32] Albert, R. et al. Microwave photon-number amplification [arXiv:2303.03173](https://arxiv.org/abs/2303.03173) (2023)
- [33] Crescini, N., Cailleaux, S., Guichard, W. et al. Evidence of dual Shapiro steps in a Josephson junction array. *Nat. Phys.* 19, 851–856 (2023).
- [34] Mehta, N., Kuzmin, R., Ciuti, C. et al. Down-conversion of a single photon as a probe of many-body localization. *Nature* 613, 650–655 (2023). <https://doi.org/10.1038/s41586-022-05615-y>
- [35] Devoret, M. H. et al. Effect of the electromagnetic environment on the Coulomb blockade in ultrasmall tunnel junctions. *Phys. Rev. Lett.* 64, 1824–1827 (1990).
- [36] "Single Charge Tunneling", edited by H. Grabert and M. H. Devoret, NATO ASI Series B, Vol. 294, pp. 21-107 (Plenum Press, New York, 1992).
- [37] Souquet, JR., Woolley, M., Gabelli, J. et al. Photon-assisted tunnelling with nonclassical light. *Nat Commun* 5, 5562 (2014).
- [38] Jin, Y. et al., "Ultra-low noise CryoHEMTs for cryogenic high-impedance readout electronics: Results and applications," 2016 13th IEEE International Conference on Solid-State and Integrated Circuit Technology (ICSICT), Hangzhou, China, 2016, pp. 342-345, doi: 10.1109/ICSICT.2016.7998915.
- [39] Schoelkopf, R.J. et al. The Radio-Frequency Single-Electron Transistor (RF-SET): A Fast and Ultrasensitive Electrometer. *Science* 280, 1238-1242 (1998). DOI:10.1126/science.280.5367.1238

Sample Fabrication and Experimental setup

The sample shown in figure 1 of the main text is fabricated via a three steps process using standard e-beam and optical lithography techniques on an oxidized silicon wafer. We first write by e-beam lithography a narrow (720 nm) and long (180 μm) nanowire. Then we evaporate a thin (20 nm) film of granular aluminum. In a second step we draw by e-beam lithography the design for a small (140 nm \times 120 nm) Al-based superconducting tunnel junction that we evaporate using the Manhattan technique with three successive oxidation steps to obtain

a large normal state resistance. In the last step we use optical lithography to draw and evaporate 100 nm of aluminum to realize a 50 Ω microstrip transmission line and connect the tunnel junction and the grAl with a patch.

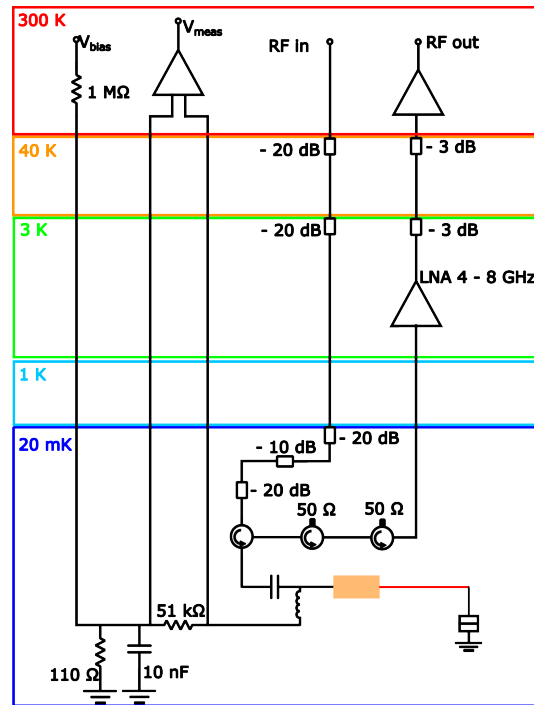


FIG. S1. Detailed experimental setup

The device is mounted in a copper box equipped with a microwave printed circuit board. The box is sealed and anchored to the mixing chamber plate of a dilution fridge with a base temperature of 20 mK. The experimental setup is shown in figure S1. In order to dc-bias the junction and do microwave measurements concurrently, the device is connected to the rest of the measurement circuit through a diplexer or a bias tee. The microwave measurements were carried out with a vector network analyzer. The excitation is delivered to the device through an attenuated line, and the reflected signal is directed to the output line using a series of circulators. The reflected signal is amplified first by a low temperature HEMT amplifier anchored at 4 K, and then by two room temperature amplifiers. At the same time, the junction is voltage biased using a voltage divider and a filtering capacitor connected to the low frequency port of the diplexer/bias-tee at base temperature. Current through the junction is measured by the voltage drop across a 51.6 k Ω resistor connected in series with the device. The voltage is amplified using a NF LI-75A differential preamplifier, prior to being further amplified and filtered by a Stanford Research SR560 amplifier. The gain of this measurement chain, as well as the measurement resistor has been calibrated in a separate cooldown. The input impedance of the preamplifier was measured independently to be (94.8 ± 0.2) M Ω .

Resonator Characterization

The quarter wavelength granular aluminum (grAl) resonator is designed such that the fundamental resonance is close to 6 GHz with a characteristic impedance of approximately 5 k Ω . In order to characterize the resonator, we measure its resistance in the normal state as function of temperature during the cooldown. Just above the superconducting transition, we obtain (243 ± 3) k Ω . Knowing the wire dimensions (180 μm long, and 720 nm wide), we obtain the sheet resistance of the grAl layer to be $R_{\square} = (970 \pm 20) \Omega/\square$, which corresponds to a resistivity of $(1940 \pm 40) \mu\Omega \text{ cm}$. Using Mattis-Bardeen theory in the low temperature limit, the expected sheet inductance is $L_{\square} = \hbar R_{\square}/(\pi \Delta_{\text{grAl}})$, where $\Delta_{\text{grAl}} = 330 \mu\text{eV}$ is the grAl superconducting gap, which we independently measure using tunneling spectroscopy. We obtain a sheet kinetic inductance $L_{\square} = (618 \pm 10) \text{ pH}/\square$.

We simulate the electromagnetic properties of the resonator using a simple transfer matrix method. We input the sheet inductance determined above and the capacitance per unit length that we determine to be 41.7 pF m $^{-1}$ from finite element simulations using the Sonnet Software. We calculate the resonant modes by supposing that the grAl resonator is terminated by a capacitor representing the junction. The first two modes are experimentally measured to resonate at $\omega/2\pi = 5.52$ GHz, and $\omega_2/2\pi = 17.8$ GHz. The junction capacitance is chosen such that these values are reproduced by the model. This capacitance is 2.6 fF, which is compatible with the 120 nm \times 140 nm junction and the 20 $\mu\text{m} \times$ 20 μm patching pad, which connects the junction to the resonator. Using the same parameters, we compute the resonant frequencies of the higher modes, as well as their impedance, and coupling parameter. The results are given in the table below:

Mode	$\omega/2\pi$ (GHz)	Z_c (k Ω)	λ
1	5.52	5.09	0.79
2	17.77	0.77	0.31
3	31.39	0.20	0.16
4	45.59	0.07	0.09
5	60.04	0.03	0.06
6	74.59	0.02	0.05
7	89.21	0.01	0.04

Junction Characterization

The previous model also predicts a value for the coupling loss rate, which is $\kappa_c/2\pi \approx 78$ MHz. As explained in the main text, we need to match this rate to the junction loss rate (see equation 1 in the main text). A junction with a normal state resistance of $R_N \approx 2\Delta\lambda^2 e^{-\lambda^2}/\kappa_c = 1.6$ M Ω should satisfy this condition, where the superconducting gap of aluminum is $\Delta = 203 \mu\text{eV}$. We measure

the resistance of the junction on the sample to be 1.53 M Ω far above the gap, which is close to the desired value.

The effective resistance that enters the calculation of the different photo-assisted tunneling rates with the fundamental mode must be corrected for the dynamical Coulomb blockade factors due to the higher modes. We suppose that these modes remain in vacuum, and we renormalize the tunnel resistance of the junction compared to the value measured at high bias voltage as

$$R_T = \prod_{n \neq 1} |\langle 0 | e^{i\lambda_n (a_n + a_n^\dagger)} | 0 \rangle|^2 \times 1.53 \text{ M}\Omega \quad (\text{S.1})$$

$$= e^{-(\lambda_2^2 + \lambda_3^2 + \dots)} \times 1.53 \text{ M}\Omega \quad (\text{S.2})$$

The resulting resistance $R_T = 1.75$ M Ω is used in all our simulations.

In order to compute the tunneling rates and Lamb shifts that appear in the quantum master equation, we have to model the $I(V)$ characteristic of the junction in the absence of the mode that is considered in the master equation (here the fundamental mode). To this purpose, we use the standard formula

$$I(V) = \frac{1}{eR_T} \int_{-\infty}^{\infty} n_L(E) n_R(E+eV) (f(E) - f(E+eV)) dE \quad (\text{S.3})$$

where $f(E)$ is the Fermi distribution, and n_L and n_R are the dimensionless quasiparticle density of states of the left and right junction electrodes:

$$n(E) = \text{Re} \left(\frac{E + i\Gamma}{\sqrt{(E + i\Gamma)^2 - \Delta^2}} \right) \quad (\text{S.4})$$

The density of states is parametrized through the gap Δ and the Dynes parameter Γ . In our experiment, this parameter is too small to be reliably determined, therefore we consider $\Gamma = 0.01 \mu\text{eV}$, which has negligible influence on the results but eases the numerical convergence of the integral. We extract the gap value $\Delta = 203 \mu\text{eV}$ from the measured current-voltage characteristic of the junction (see figure 3 in the main text).

Quantum Master Equation and Power Calibration

In order to describe the resonator coupled to the junction, we consider a quantum master equation as detailed in [1]. The coupling between the resonator mode and the junction results in an irreversible energy exchange, which is represented by quantum jumps, and in a Lamb shift of the resonator eigenstates. Quantum jump operators A_l , which describe the non-unitary evolution of the system, create (annihilate) l ($-l$) photons in the resonator for $l > 0$ ($l < 0$). The jump operators are given in Fock-

state basis by [2]:

$$\langle n+l | A_l | n \rangle = \left(\frac{n!}{(n+l)!} \right)^{1/2} (i\lambda)^l e^{-\lambda^2/2} L_n^{(l)}(\lambda^2), \quad l \geq 0 \quad (\text{S.5})$$

where $L_n^{(l)}$ are the generalized Laguerre polynomials. Operators A_l for $l < 0$ are defined as $A_{-l} = (-1)^l A_l^\dagger$. Each quantum jump operator enters the master equation with a corresponding jump rate, which, to a good approximation, is proportional to $I(V - l\hbar\omega/e)$, where $I(V)$ is the bare junction characteristics (see previous section). The Hamiltonian part of the evolution is governed by

$$H = H_D + H_{\text{LS}} \quad (\text{S.6})$$

$$H_D = i\eta(a - a^\dagger) - \delta a^\dagger a \quad (\text{S.7})$$

$$H_{\text{LS}} = -\frac{1}{2e} \sum_{l=-\infty}^{\infty} I^{\text{KK}}(V + l\hbar\omega/e) A_l A_l^\dagger \quad (\text{S.8})$$

where H_D describes the drive, with η being the pump rate and δ the detuning. The pump rate is related to the incident photon flux ϕ by $\eta^2 = \phi\kappa_c$. The Lamb shift term H_{LS} accounts for the frequency shift induced by the junction. Except for the attenuation factor A , which reduces the flux ϕ by an unknown amount, the other parameters entering the master equation are fixed to their *ab initio* values. The resonator loss $\kappa = \kappa_c + \kappa_i$ is taken from the mode spectroscopy (see figure 2 in the main text), the $I(V)$ characteristics of the junction is the one described in the previous section and the coupling parameter is set to $\lambda = 0.785$ as detailed above.

We look for the steady state solution of the following master equation

$$\frac{d\rho}{dt} = -i[H, \rho] + \frac{1}{e} \sum_{l=-\infty}^{\infty} I(V - l\hbar\omega/e) \mathcal{D}[A_l](\rho) + \kappa \mathcal{D}[a](\rho) \quad (\text{S.9})$$

where $\mathcal{D}[F](\rho) = F\rho F^\dagger - \frac{1}{2}\{F^\dagger F, \rho\}$, and ρ is the reduced density matrix of the resonator. The last term accounts for the damping of the resonator with a loss rate $\kappa = \kappa_c + \kappa_i$ as detailed in the main text. We assume that the thermal population of the corresponding bath is negligible. From the steady state solution ρ_s , we obtain the expected photo-assisted current through

$$I_{\text{PAT}} = \sum_{l \neq 0} I(V - l\hbar\omega/e) \text{Tr} [A_l^\dagger A_l \rho_s] \quad (\text{S.10})$$

In order to calibrate the attenuation A , we measure the photo-assisted current as a function of microwave pump power for four different junction bias voltages $eV = 2\Delta - (N - 1/2)\hbar\omega$, $N = 1, \dots, 4$. In the low pumping limit where $n_{ph} \ll 1$, we can solve the master equation analytically at the corresponding voltages by truncating it to the lowest $N + 1$ Fock states and by neglecting the different energy shifts. To lowest order in

η , the photo-assisted current calculated is:

$$I_{\text{PAT}}^{(1)} = \frac{4\eta^2 \kappa_j^{(1)} e}{(\kappa + \kappa_j^{(1)})^2} \quad (\text{S.11})$$

$$I_{\text{PAT}}^{(2)} = \frac{32\eta^4 \kappa_j^{(2)} e}{\kappa^2 (2\kappa + \kappa_j^{(2)})^2} \quad (\text{S.12})$$

$$I_{\text{PAT}}^{(3)} = \frac{96\eta^6 \kappa_j^{(3)} e}{\kappa^4 (3\kappa + \kappa_j^{(3)})^2} \quad (\text{S.13})$$

$$I_{\text{PAT}}^{(4)} = \frac{512\eta^8 \kappa_j^{(4)} e}{3\kappa^6 (4\kappa + \kappa_j^{(4)})^2} \quad (\text{S.14})$$

$$\text{with } \kappa_j^{(n)} = \frac{e^{-\lambda^2} \lambda^{2n} I(2\Delta/e + \hbar\omega/2e)}{n! e} \quad (\text{S.15})$$

where $I_{\text{PAT}}^{(N)}$ stands for the photo-assisted current at $eV = 2\Delta - (N - 1/2)\hbar\omega$. As $\eta^2 \propto A$, fitting these four currents is equivalent to simultaneously fitting A, A^2, A^3 and A^4 , which allows us to precisely calibrate A . Figure S2 shows the predictions of the analytical formula together with the data. As can be seen, the validity domain of the analytical formula is too restricted, which is why we rather use the numerical solution of the master equation [4] in order to obtain a more precise fit as shown in the figure 3 of the main text. From this method, the estimated attenuation is $A = 107$ dB.

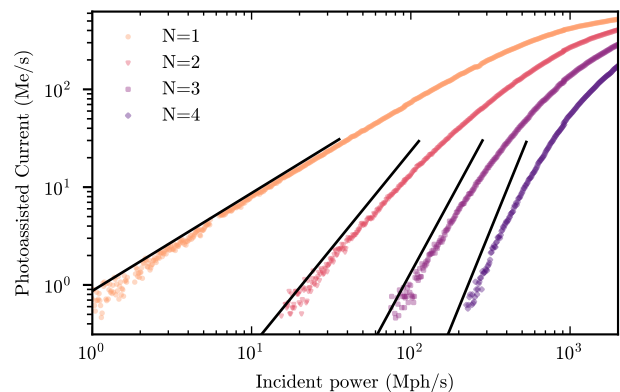


FIG. S2. Photo-assisted current as a function of pump power for bias voltages $eV = 2\Delta - (N - 1/2)\hbar\omega$, $N = 1, \dots, 4$ (same data as in figure 3 of the main text). Black solid lines are analytic predictions obtained by expanding the solution of the master equation at low power (equations (S.11) to (S.14)).

Other Methods of Calibration

We have verified that two other calibration methods give consistent results with the method detailed in the previous section. We first estimate the attenuation of

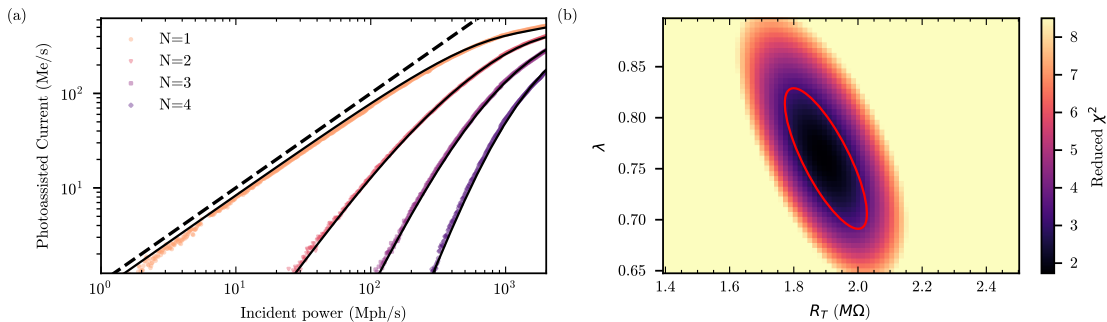


FIG. S3. (a) Fit of the photo-assisted current measured at bias voltages $eV = 2\Delta - (N - 1/2)\hbar\omega$, $N = 1, \dots, 4$ (same data as in figure 3 of the main text), but λ and R_T are now free fit parameters. The dashed line represents ideal quantum efficiency. (b) Reduced χ_r^2 as a function of λ , and R_T . For each value of these two parameters, we obtain a fitted attenuation and a reduced χ_r^2 . By considering the region where χ_r^2 remains below two times its minimal value (red ellipse), we obtain an estimation of the error on the attenuation from the standard deviation of the different attenuation results.

every microwave component and cable and obtain a total attenuation of 106 dB. This method relies on many assumptions and cannot be considered as reliable. We also consider the shot-noise emission of the junction at a large bias voltage as a calibrated source that allows us to know the gain of the amplification chain, from which we obtain the attenuation by measuring the reflected power outside the resonance.

At sufficiently high bias compared to the gap, where the current I through the junction can be approximated as being proportional to V , the noise power emitted by the junction in a bandwidth BW centered at the resonant frequency of the resonator is [3]

$$P = \frac{4\lambda^2 \kappa_c \hbar \omega I}{e(\kappa + \omega \lambda^2 R_N / \pi R_K)^2} \times BW \quad (\text{S.16})$$

where R_N is the junction resistance given by $R_N = V/I$. We measure the emitted power in a 5 MHz bandwidth around resonance between 1.3 mV and 1.8 mV, which increases linearly with V as expected. By comparing the slope to equation S.16, we obtain the gain of our measurement chain, from which we deduce an attenuation of (107 ± 1) dB.

Quantum Efficiency Error Estimation

Once the attenuation of the incoming photon flux is known, the quantum efficiency is directly obtained from the linear increase of the photo-assisted current as a function of flux. As stated in the main text, we obtain a quantum efficiency of 0.83 with negligible statistical error given the negligible noise on the current as seen in figure 3 of the main text. The main source of error is the systematic error that enters the calibration of the attenuation. In particular, we have to know the effective resistance R_T , which includes the effect of dynamical Coulomb blockade of all the higher modes that we

cannot characterize experimentally. In order to estimate the effect of this error, we let R_T and λ be free fit parameters in the calibration procedure. We then obtain $\lambda = 0.76$, $R_T = 1.90$ M Ω and $A = 106.7$ dB, which results in a quantum efficiency of 0.79. With these extra fit parameters, the reduced χ_r^2 is below 2, which indicates that it can be used to estimate the error bar on the fit parameters. By considering the region where the reduced χ_r^2 is doubled compared to the optimal point as our uncertainty region (see figure S3), we obtain a 1σ error bar of 0.05 on the quantum efficiency, which is the value of the error stated in the main text.

Dark Current

Dark current is a key figure of merit for a photon detector. In order to obtain its value, we measure the current through the junction close to the gap in absence of any microwave drive. This measurement is shown in figure S4.

We observe two steps, which indicate the presence of a residual photon population in the first two modes. The voltage width of the steps (see figure S4) matches the fundamental resonator mode at 5.525 GHz, and the one of the next mode at 17.8 GHz. In the working window of our detector ($2\Delta - \hbar\omega < eV < 2\Delta$), the dark current is approximately 55 fA, which corresponds to a population of $1.5 \cdot 10^{-3}$ in the fundamental mode as can be seen also in figure 4 of the main text.

* julien.basset@universite-paris-saclay.fr

[1] J. Estève, M. Aprili, and J. Gabelli, *Quantum dynamics of a microwave resonator strongly coupled to a tunnel junction*. arXiv:1807.02364 (2018)

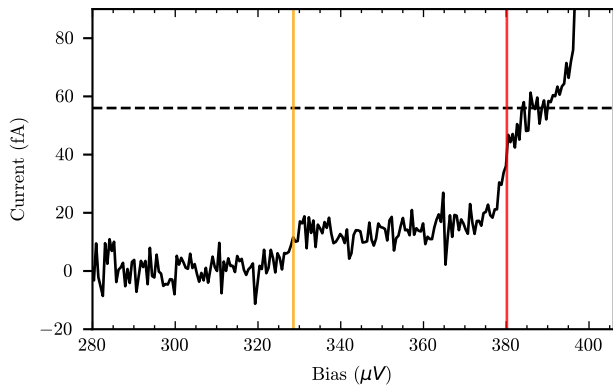


FIG. S4. $I(V)$ characteristic of the junction at 20 mK in the absence of any microwave drive. Two steps are still visible, corresponding to the 17.8 GHz mode (orange line), and the fundamental mode (red line).

- [2] Cahill, K.E., Glauber, R.J., Ordered Expansions in Boson Amplitude Operators. *Phys. Rev.* 177, 1857–1881. (1969).
- [3] Ménard, G.C., Peugeot, A., Padurariu, C., Rolland, C., Kubala, B., Mukharsky, Y., Iftikhar, Z., Altimiras, C., Roche, P., Le Sueur, H., Joyez, P., Vion, D., Esteve, D., Ankerhold, J., Portier, F., 2022. Emission of Photon Multiplets by a dc-Biased Superconducting Circuit. *Phys. Rev. X* 12, 021006. (2022)
- [4] J. R. Johansson, P. D. Nation, and F. Nori: "QuTiP 2: A Python framework for the dynamics of open quantum systems.", *Comp. Phys. Comm.* 184, 1234 (2013)